



Rupture behaviors of the southern Xianshuihe fault and seismicity around Mt. Gongga: Insights from the 2022 M_W 6.6 Luding (China) earthquake sequence

Wenzheng Gong^a, Lingling Ye^{a,b,*}, Shiqing Xu^{a,*}, Yipei Tan^c, Xiaofei Chen^a

^a Department of Earth and Space Sciences, Southern University of Science and Technology, Shenzhen 518055, China

^b Guangdong Provincial Key Laboratory of Geophysical High-resolution Imaging Technology, Southern University of Science and Technology, Shenzhen 518055, China

^c Tianjin Earthquake Agency, Tianjin 300201, China

ARTICLE INFO

Keywords:

2022 Luding Earthquake
Xianshuihe Fault
Moxi Segment
Mt. Gongga
Fluid Flow

ABSTRACT

The 2022 M_W 6.6 Luding earthquake occurred on the Moxi segment of the Xianshuihe fault at the southeast margin of Tibetan Plateau, China. To assess the seismic potential of the Moxi segment, we examine the rupture process of the mainshock and aftershock sequence, along with historical seismicity. Our preferred slip model inverted from teleseismic body waves and regional GNSS static displacements shows a dominant southeastward rupture consisting of two distinct, prominent slip patches along strike extending by ~ 15 km, with a peak slip of ~ 2.8 m, approximately balancing the slip deficit since the last major earthquake in 1786. The northern section of the Moxi segment experienced minor coseismic slip, which, together with the significant slip deficits and positive Coulomb failure stress change induced by the 2022 mainshock indicates a high seismic potential. Several aftershock clusters are distributed along or near the Moxi segment, with strike-slip focal mechanisms around the downdip edge of the coseismic slip area at ~ 8 –12 km. At the eastern flank of Mt. Gongga, another cluster of normal faulting aftershocks is located at shallower depths of ~ 3 –7 km, with high seismicity rate over ~ 9 months including two other M_5 sequences in January and February 2023. Similar intense shallow normal faulting activity had occurred after the impoundment of the nearby Dagangshan reservoir in 2015. We speculate that some NW-SE trending normal faults were initially developed by the gravitational collapse of Mt. Gongga underneath the eastern flank, further weakened by fluid flow, as supported by the existence of hot springs and water impoundment, and reactivated by the tensional stress change induced by the 2022 mainshock. These results have important implications for assessing the seismic hazard in and around the Moxi segment, and the potential interplay between strike-slip fault and nearby mountain areas.

1. Introduction

On 5 September 2022 at 12:52:18 (Beijing time, UTC+8), an M_W 6.6 strong earthquake struck the Luding County region in Sichuan Province, southwest China [hypocenter at (29.59°N, 102.09°E, 16.0 km) from the China Earthquake Network Center (CENC) catalog]. It occurred in mountain areas near Mt. Gongga with noticeable surface rupture and triggered more than 5000 landslides with a total area of ~ 28 km² (An et al., 2023; Chen et al., 2023; Dai et al., 2023). The event caused 117 deaths or missing and 3275 injuries, with an estimated damage loss of 15.48 billion CNY (Department of Emergency Management of Sichuan Province (<https://yjt.sc.gov.cn/scyjt/juecegongkai/2022/10/28/db7c636b4a4e44adaf345a388344f3a7.shtml>)).

The 2022 Luding earthquake occurred on the Moxi segment in the southernmost part of the left-lateral strike-slip Xianshuihe fault, near the Y-shaped junction intersected by the Anninghe and Longmenshan faults (Fig. 1). The Xianshuihe fault is along the southeast margin of the Tibetan Plateau in China, as the boundary between the Bayan Har block and the Sichuan-Yunnan block. It is one of the most active faults in China, with a relatively high strike-slip slip rate of ~ 1.0 cm/yr (Allen et al., 1991; Bai et al., 2018, 2021; Li et al., 2021). Since 1700, 18 $M_{6.0+}$ and 8 $M_{7.0+}$ earthquakes have occurred on the Xianshuihe fault, covering the whole fault with a total rupture length of ~ 350 km (Allen et al., 1991; Wen et al., 2008; Fig. 2). In history, the 1327 $M_{7.5}$ ($7\frac{1}{2}$) and 1786 $M_{7.8}$ ($7\frac{3}{4}$) earthquakes ruptured the Moxi segment with a similar

* Corresponding authors at: Department of Earth and Space Sciences, Southern University of Science and Technology, Shenzhen 518055, China.

E-mail addresses: yell@sustech.edu.cn (L. Ye), xusq3@sustech.edu.cn (S. Xu).

<https://doi.org/10.1016/j.tecto.2024.230538>

Received 17 April 2024; Received in revised form 14 October 2024; Accepted 16 October 2024

Available online 18 October 2024

0040-1951/© 2024 Elsevier B.V. All rights reserved, including those for text and data mining, AI training, and similar technologies.

spatial extent of ~ 90 km (Wen et al., 2008), indicating a seismic cycle with a recurrence time of 459 years. There have been no recorded $M_{6.0+}$ earthquakes since the 1786 $M_{7.8}$ event, so this segment is called the Moxi seismic gap (Shao et al., 2023; Zhang et al., 2023a). Published coseismic slip models for the 2022 Luding earthquake (e.g., Li et al., 2022; Yang et al., 2022; Guo et al., 2023; Han et al., 2023; Liang et al., 2023; Zhang et al., 2023a; Zhang et al., 2023b; Zhao et al., 2023; Zou et al., 2024) all indicate an overall asymmetrical rupture propagation primarily toward the southeast along strike. However, these models exhibit noticeable differences in detail, depending on the datasets and smoothness applied in the analysis. Some models inverted from teleseismic body wave data and/or near-field strong motion data predominantly exhibit two distinct slip patches (e.g., Zhao et al., 2023; Zhang et al., 2023a), while Li et al. (2022) obtain a coseismic slip model with more distinct slip patches with GNSS and InSAR data. Other models with InSAR data show a relatively smooth coseismic slip distribution (e.g., Guo et al., 2023; Han et al., 2023; Liang et al., 2023; Zou et al., 2024).

The 2022 M_W 6.6 Luding mainshock was not preceded by any detectable foreshocks but followed by numerous aftershocks. Over 9200 aftershocks with $M_{1.0+}$ have been detected up to 1 June 2023 from the CENC catalog. The CENC catalog and other relocation catalogs (e.g., An et al., 2023; Yang et al., 2022; Liu et al., 2023a; Zhang et al., 2023a; Zhao et al., 2023; Zhang et al., 2024) indicate that the aftershocks are distributed in distinct zones. Different from the strike-slip mainshock and aftershocks along the Moxi segment, the aftershocks in the east of Mt. Gongga (west of mainshock) exhibit normal-faulting focal mechanisms (Yang et al., 2022; Zhang et al., 2023a; Zhao et al., 2023; Zhang et al., 2024). The seismicity rate near Mt. Gongga remained high over ~ 9 months, with two other M_5 sequences in January and February 2023. However, the seismogenic structures under Mt. Gongga are still unclear. Local stress adjustment (Zhao et al., 2023) or gravitational collapse (Zhang et al., 2024) due to the vertical movement of Mt. Gongga are suggested to cause extensive normal faulting. The historical seismicity in the east of Mt. Gongga was relatively low before 2015, but

significantly increased with the impoundment of nearby Dagangshan reservoir (Feng et al., 2018). The spatiotemporal distribution of intense seismicity calls for further investigation of the seismogenic structure and mechanism underneath the eastern flank of Mt. Gongga.

To understand the seismic potential and faulting characteristics around the Moxi segment, we first invert for the coseismic slip distribution of the 2022 Luding mainshock using teleseismic body waves and the regional GNSS static displacement measurements. Then, we evaluate the slip budget using the historical earthquake catalog and calculate the change of Coulomb failure stress (Δ CFS) induced by the mainshock. We invert for focal mechanisms of $M_{3.0+}$ events using the regional broadband seismic recordings and confirm the diverse faulting styles in different aftershock zones. Finally, we combine geological observations and focal mechanisms to elucidate the mechanism for the frequent intense shallow seismicity underneath the eastern flank of Mt. Gongga.

2. Quantifying the 2022 M_W 6.6 Luding mainshock

2.1. Point-source solutions

Several agencies reported the point-source moment tensor solutions of the 2022 Luding mainshock using global teleseismic waveforms or regional seismic recordings (Table 1). The long-period W -phase solution by the U.S. Geological Survey National Earthquake Information Center (USGS-NEIC) has a double-couple solution with strike $\varphi = 345^\circ$, dip $\delta = 88^\circ$, and rake $\lambda = 17^\circ$, seismic moment $M_0 = 1.158 \times 10^{19}$ Nm (M_{WW} 6.64), and centroid depth at 15.5 km. The Global Centroid Moment Tensor (GCMT) solution, based on a dataset of 439 body waves, 374 mantle waves, and 449 surface waves lowpass filtered at periods of 50, 125, and 50 s, respectively, has the best double-couple solution with strike $\varphi = 164^\circ$, dip $\delta = 78^\circ$, and rake $\lambda = 7^\circ$, seismic moment $M_0 = 1.2 \times 10^{19}$ Nm (M_W 6.7), and centroid depth at 18.0 km. The Institute of Geophysics, China Earthquake Administration (IGP-CEA) obtained a double-couple solution based on regional broadband station

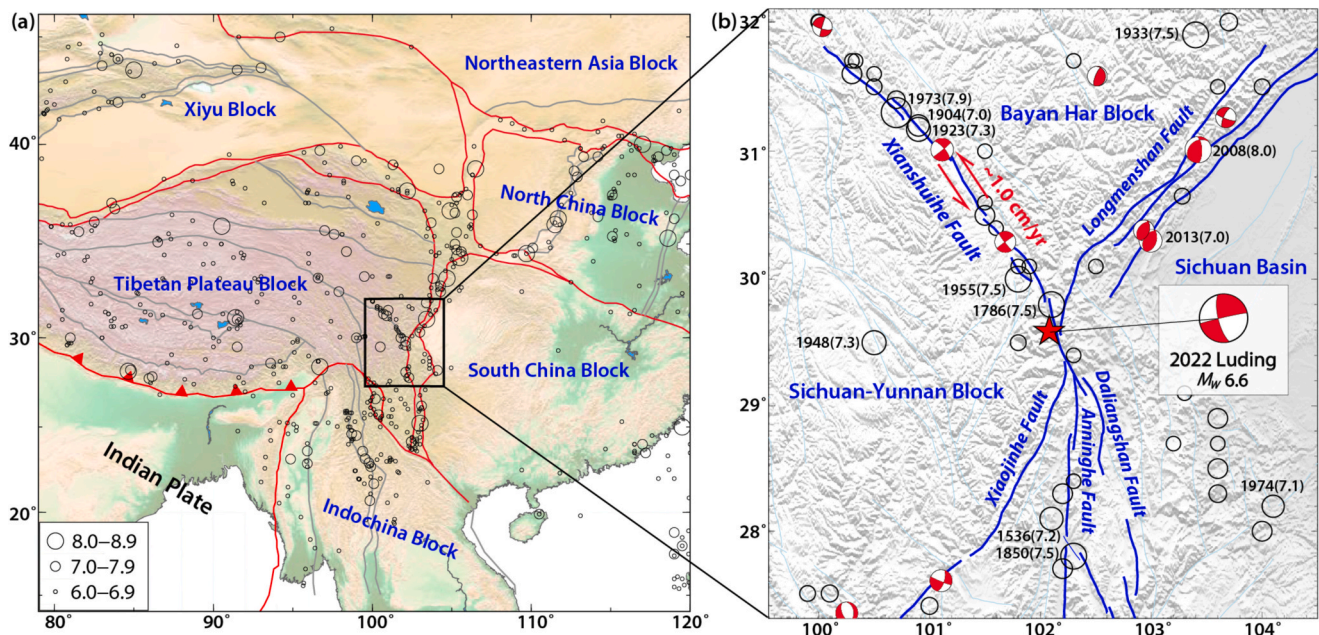


Fig. 1. Tectonic context and historical strong earthquakes surrounding the 2022 M_W 6.6 Luding earthquake. (a) The map shows the primary and secondary active tectonic blocks in and around China, outlined by red and gray curves (Zhang et al., 2003). Historical events with $M_{6.0+}$ since 186 BCE from the China Earthquake Network Center (CENC) catalog are denoted by circles. (b) The fault system and historical strong earthquakes around the 2022 Luding earthquake. Major active faults in the southeastern Tibetan Plateau are delineated by blue curves, with a slip rate of ~ 1.0 cm/yr for the Xianshuihe fault (Allen et al., 1991; Bai et al., 2018; 2021; Li et al., 2021). Circles show $M_{6.0+}$ earthquakes from 1216 to 1976 from the CENC catalog. Focal mechanisms show $M_{6.0+}$ events from the Global Centroid Moment Tensor (GCMT) catalog since 1976. The red star marks the epicenter of the 2022 mainshock from the CENC catalog with the focal mechanism from the CAP (Cut-and-Paste) inversion. (For interpretation of the references to colour in this figure legend, the reader is referred to the web version of this article.)

recordings using the Cut-and-Paste (CAP) method (Zhao and Helmberger, 1994; Zhu and Ben-Zion, 2013; Bai et al., 2020), with strike $\varphi = 343^\circ$, dip $\delta = 89^\circ$, rake $\lambda = -24^\circ$, moment magnitude M_W 6.7, and centroid depth at 7.0 km. IGP-CEA also reported a double-couple solution based on teleseismic body waves with strike $\varphi = 163^\circ$, dip $\delta = 77^\circ$, rake $\lambda = -5^\circ$, seismic moment $M_0 = 1.039 \times 10^{19}$ Nm (M_W 6.61), centroid location at (120.14°E, 29.55°N), and centroid depth at 16.0 km.

Given the variations in centroid depth and strike among these solutions, we perform a point-source inversion using the CAP method that we slightly modified (Gong et al., 2022) with the regional seismic recordings within ~ 500 km from 30 broadband stations from ChinArray (Fig. A1; Zheng et al., 2010). The P and S waveforms are bandpass filtered at 0.01 - 0.15 Hz and 0.01 - 0.10 Hz, respectively. We use the average local seismic velocity model near the epicenter for the inversion, modified from Liu et al. (2023b) (Fig. A2). The focal mechanism is inverted for point sources with variable source durations, locations, and depths. In our modified CAP inversion (Gong et al., 2022), we use an isosceles triangle to approximate the shape of the source time function and grid search the centroid time to get the source duration, similar to that used in the typical long-period W phase inversion as implemented by USGS-NEIC and the GCMT solution. The result is summarized in Fig. A1. It has a best double-couple solution for one nodal plane with strike $\varphi_1 = 167^\circ$, dip $\delta_1 = 73^\circ$, rake $\lambda_1 = -1^\circ$, and the other with strike $\varphi_2 = 257^\circ$, dip $\delta_2 = 89^\circ$, rake $\lambda_2 = -163^\circ$. The inverted seismic moment M_0 is 1.054×10^{19} Nm (M_W 6.62). The optimal search results in a relatively shallow centroid depth of 7 km at the centroid location (120.08°E, 29.54°N), south of the epicenter, suggesting a southeastward rupture. The centroid time is about 6.0 s, indicating the source time duration is about 12 s. Considering the northwest-southeast trend of the Moxi segment, we choose the plane with strike $\varphi = 167^\circ$ and dip $\delta = 73^\circ$, rather than the northeast-trending nodal plane, as the fault plane for the mainshock rupture.

2.2. Finite-fault slip distribution

We use teleseismic and geodetic observations to invert the space-time history of rupture for the 2022 Luding mainshock. The seismological dataset includes 59 P waves and 27 SH waves with good azimuthal distribution. The broadband seismic waveform recordings are corrected by removing instrument response, bandpass filtered in the frequency band of 0.005-0.9 Hz, and integrated to ground displacement for inversion. The geodetic data are from Li et al. (2022), which includes 74 stations with horizontal coseismic static ground displacements within ~ 200 km, and the closest station is ~ 16 km northeast of the epicenter with a horizontal displacement of ~ 10 cm.

We perform a joint, least-squares kinematic finite-fault inversion with moment constraint (Hartzell and Heaton, 1983; Kikuchi and Kanamori, 1991; Ye et al., 2016). We assume a planar-fault model with fixed strike $\varphi = 167^\circ$, dip $\delta = 73^\circ$, while allowing rake to vary within each subfault. The source time functions for each subfault are parameterized by overlapping triangular functions that provide flexibility in the specific time history for each subfault. We set up 20 grids along strike and 10 grids along dip with each subfault of $2.0 \text{ km} \times 2.0 \text{ km}$ and 8 triangles with 1-s rise-time offset by 1 s for source time function which gives a possible total subfault duration of 9 s. We use the average local seismic velocity model near the epicenter modified from Liu et al. (2023b) with the inferred density based on the empirical relationship by Brocher (2005) to calculate Green's function.

Because of the large variations of inferred dip angle in published studies, we test four planar-fault models with dip $\delta = 70^\circ$, $\delta = 75^\circ$, $\delta = 80^\circ$, and $\delta = 85^\circ$ and find an optimal dip angle of $\delta = 73^\circ$ from our regional CAP inversion. For these planar-fault models with dip $\delta = 75^\circ$, $\delta = 80^\circ$, $\delta = 85^\circ$, the initial parts of teleseismic P waves at the stations with azimuths of 254° - 315° near P radiation nodes (such as KIBK, IKL, and XBFO) are not well modeled, with opposite polarity for synthetics and observations (Fig. A3). The waveform fits are good for the solution dip $\delta = 70^\circ$, so we prefer the planar-fault model with a relatively small dip, δ

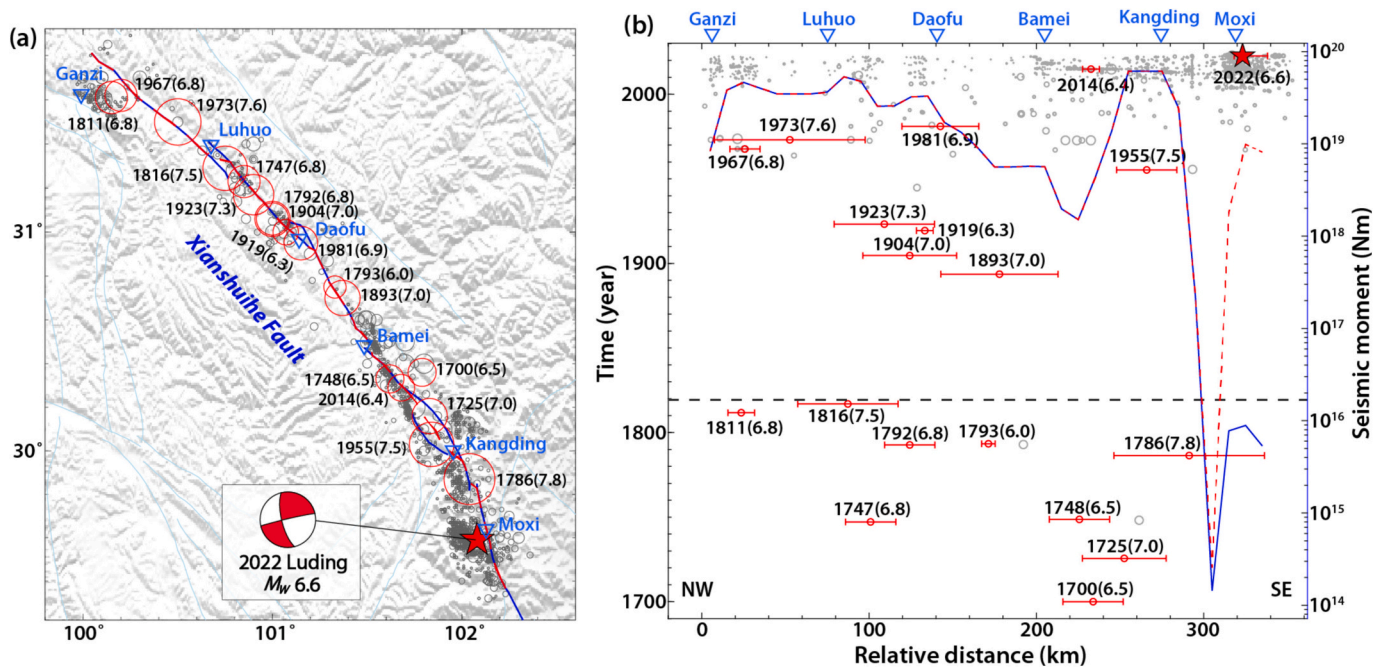


Fig. 2. Historical moderate-to-major earthquakes and slip budget along the Xianshuihe fault. (a) Historical seismicity from 1700 to 2022 within a distance of 20 km of the Xianshuihe fault. The red and gray circles are the $M_{6.0+}$ earthquakes from Wen et al. (2008) and events with magnitude from 1.0 to 6.0 from the CENC catalog, respectively. (b) The projection of seismicity along the Xianshuihe fault. The horizontal bars show the rupture extent for major earthquakes from Wen et al. (2008) and for the 2022 Luding earthquake of this study. The blue and dashed red curves show the accumulated seismic moment calculated in 10-km bins along the Xianshuihe fault before and after the 2022 Luding sequence since 1816, respectively. (For interpretation of the references to colour in this figure legend, the reader is referred to the web version of this article.)

Table 1
Point-source solutions for the 2022 Luding mainshock.

	Lon.	Lat.	Depth (km)	T_c (s)	Strike	Dip	Rake	M_0 ($\times 10^{19}$ Nm)	M_w
USGS-NEIC	102.01°	29.53°	15.5	6.5	345°	88°	17°	1.158	6.64
GCMT	102.24°	29.50°	18.0	5.4	164°	78°	7°	1.200	6.70
IGP-CEA (regional data)	102.08°	29.59°	7.0	–	343°	89°	-24°	1.396	6.70
IGP-CEA (teleseismic data)	120.14°	29.55°	16.0	5.0	163°	77°	-5°	1.039	6.61
This study	120.08°	29.54°	7.0	6.0	167°	73°	-1°	1.054	6.62

= 73°. Compared to teleseismic data, GNSS static displacement data are more sensitive to the absolute distribution of coseismic slip, so the absolute location of the hypocenter is crucial in the joint inversion. Zhang et al. (2023a) use the S - P arrival time differences at two stations near the epicenter (2.0 km and 6.6 km) and show a shallow source depth <10 km. Here, we test several models with different source depths varying from 8 km to 14 km. The waveform fits at the stations with azimuths of 288°–336° (such as EIL, GNI, and KEV) are bad for the models with source depths of 14 km and 12 km (Fig. A4). Models with shallow source depths ≤ 10 km improve the fitting. Ultimately, we set a source depth of 6.8 km and extend the model dimension to reach the ground surface with the dip angle of 73° at the epicenter (120.102°E, 29.590°N). The epicenter slightly deviates from that given by CENC to ensure a spatial match between the surface rupture from the field observation (Li et al., 2023). The maximum rupture propagation speed in the inversion is set as 2.8 km/s which results in a good match with locations of surface rupture.

The final slip model is shown in Fig. 3. The moment-rate function (MRF) lasts for ~ 14.0 s, with a centroid time of 6.7 s, slightly larger than the centroid time of 6.0 s in our point-source CAP inversion. The rupture mainly propagates to the southeast along strike with a peak slip of ~ 2.8 m. The slip distribution is dominated by two distinct patches extending southeastward by ~ 15 km and northwestward by ~ 5 km along strike, at depths from surface to ~ 15 km (Fig. 3c). One patch is located near the hypocenter, and another patch is distributed at a shallower area ~ 10 km to the southeast. Our slip model with an asymmetrical rupture is largely consistent with the published models (e.g., Li et al., 2022; Yang et al., 2022; Guo et al., 2023; Han et al., 2023; Liang et al., 2023; Zhang et al., 2023a; Zhang et al., 2023b; Zhao et al., 2023; Zou et al., 2024). The model fits teleseismic waveforms and regional GNSS static displacements reasonably well (Fig. 4). Some features in SH waves are not accounted for by the model due to the scattered energy. The static GNSS displacements near the rupture area are generally well fit, with

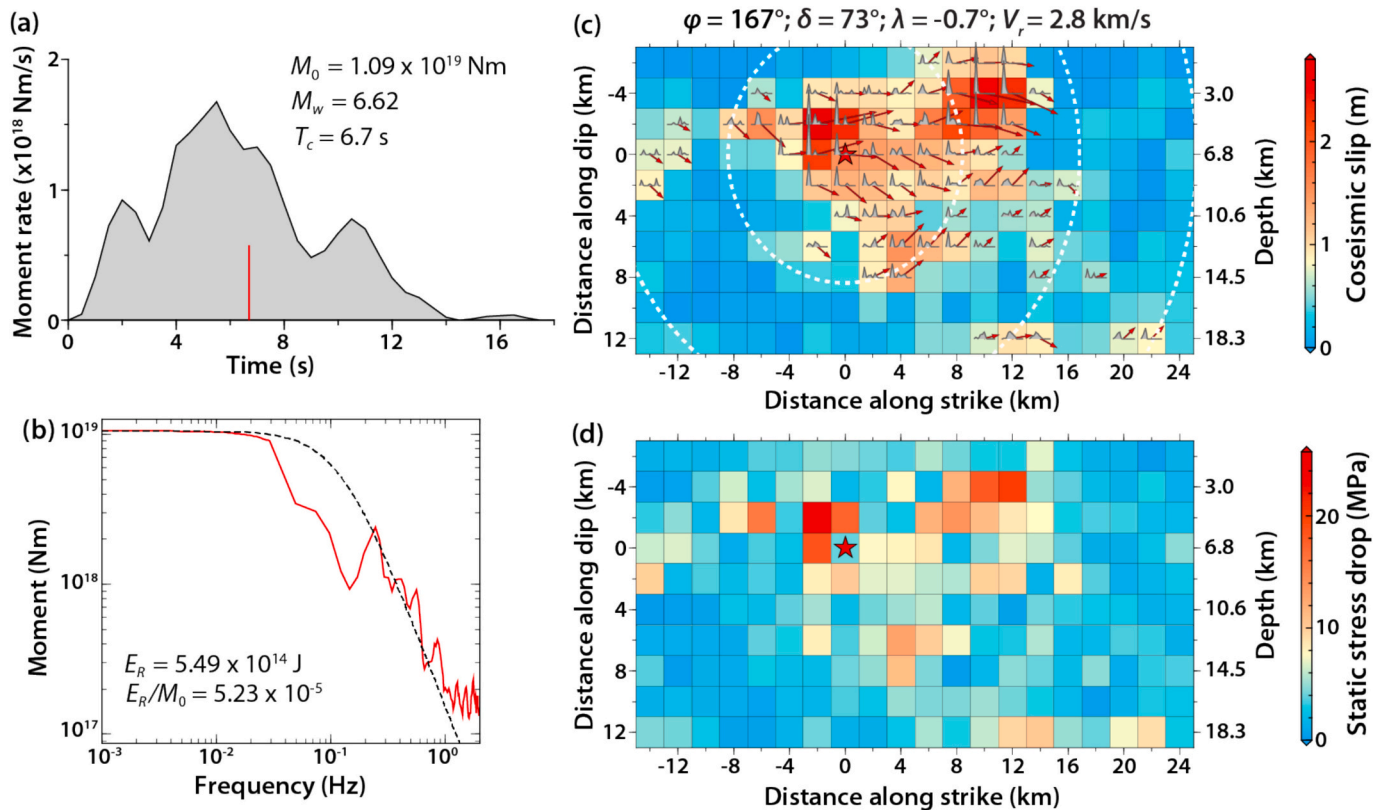


Fig. 3. Our preferred slip model for the 2022 Luding M_w 6.6 mainshock jointly inverted from teleseismic body waveforms and GNSS data. (a) Moment-rate function with centroid time indicated by the red tick. (b) Source spectrum (red curve) obtained from the moment-rate function for periods >20 s and from stacks of propagation-corrected far-field P -wave spectra for periods from 20 s to 1.0 s. The dashed curve is the reference Brune $\omega^{-2}\omega^{-2}$ spectrum with an assumed stress parameter of 3 MPa. (c) Spatial distribution of the slip model with the slip magnitude and direction shown by arrows and colors, and the gray polygons indicating source time functions for subfaults with relatively large slip. The red star shows the hypocentral location and dashed white curves indicates the rupture expansion front in 3-s intervals. (d) Spatial distribution of static stress drop calculated from the slip distribution assuming the half space (Okada, 1985; Ye et al., 2016). (For interpretation of the references to colour in this figure legend, the reader is referred to the web version of this article.)

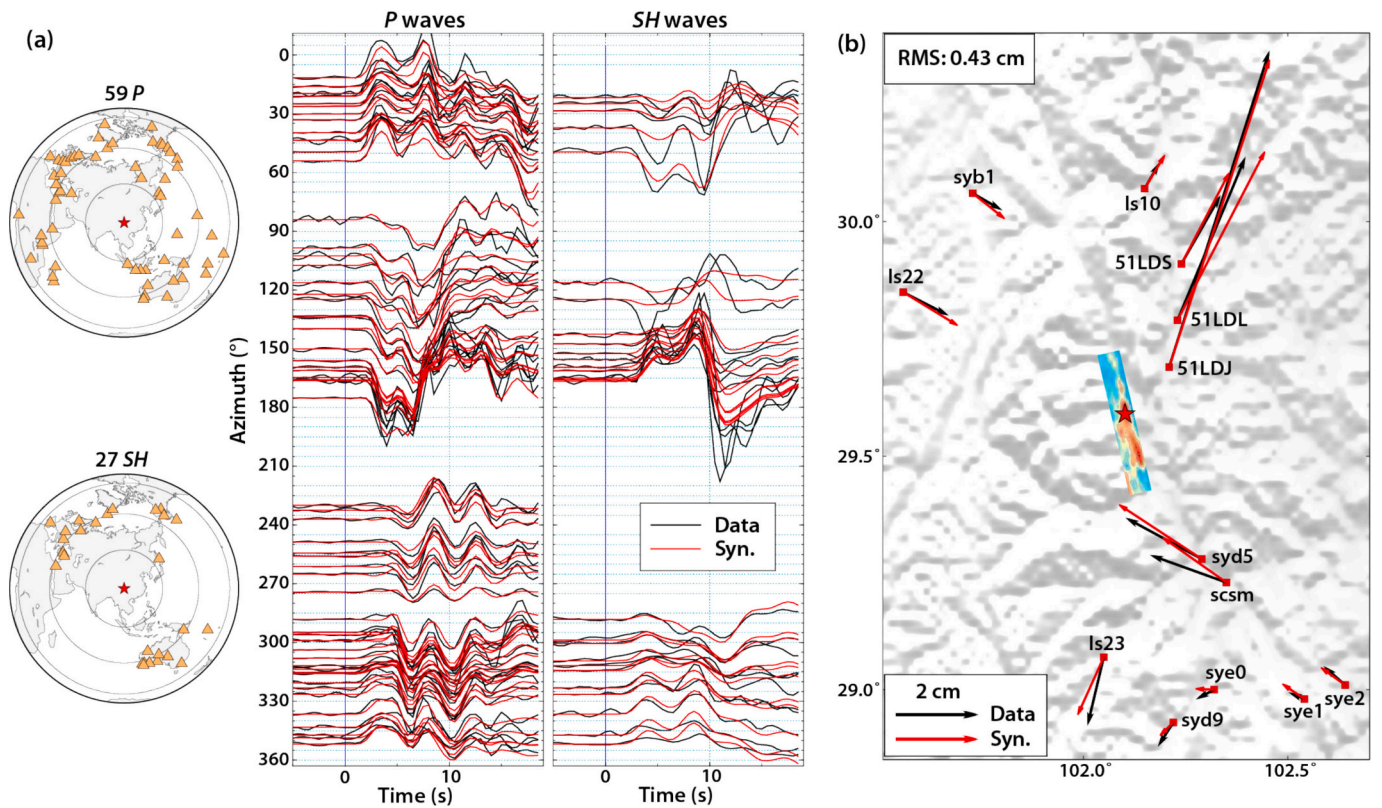


Fig. 4. Fit of teleseismic body waves and nearby GNSS displacements with our preferred slip model for the 2022 M_W 6.6 Luding earthquake (Fig. 3). (a) Comparison of observed (black) and predicted (red) teleseismic broadband P and SH waves. The station distributions in the stereographic projection for P and SH waves are shown to the left. (b) Fit of horizontal static displacement at nearby GNSS stations. The root mean square (RMS) misfit is 0.43 cm. (For interpretation of the references to colour in this figure legend, the reader is referred to the web version of this article.)

relatively large differences at some stations far away due to large observation errors (Figs. 4b and A5).

The field observation shows surface slips of ~ 50 cm, ~ 30 cm, and ~ 14 cm near the Wandong, Xingfu, and Aiguo villages (Li et al., 2023). We compare the slip models assuming different rupture speeds of 2.5 km/s, 2.8 km/s, 3.0 km/s and 3.5 km/s with the observed surface breaks (Fig. A6). The slip model with the rupture speed of 2.8 km/s shows the best match with the field observation, and is therefore taken as our preferred model (Fig. 5). In this model, the rupture to the northwest stops near three mapped E-W trending right-lateral strike-slip subfaults [Yanzigou fault (YF), Mozigou fault (MF), and Hailougou fault (HF)] that are nearly orthogonal to the left-lateral Moxi segment (Fig. 5a). These subfaults might have shattered the northern part of the Moxi segment, effectively blocking the northwestward rupture propagation. The centroid location of the finite-fault slip distribution is at (102.109°E, 29.544°N, 8.5 km depth), comparable to the centroid location (102.08°E, 29.55°N, 7.0 km) from the CAP inversion (Fig. A1). The static stress drop is 7.2 MPa for a slip-weighted estimate following Ye et al. (2016). Using the high-resolution aftershock catalog from Zhao et al. (2023), we find that aftershocks are mainly distributed in the areas with minor or no slip, at depths deeper than our coseismic slip distribution (Fig. 5b). Fig. 5c shows that few aftershocks are distributed within the large stress-drop area, indicating that the stress in the mainshock slip zone is significantly reduced to below the level that would allow for more than a few overlapping aftershocks. The enhanced stress concentration at the downdip edge induced by the mainshock rupture promotes the occurrence of aftershocks.

2.3. Source spectrum and radiated energy

The source spectrum is obtained from the moment-rate function for

periods > 20 s and from stacked broadband P wave spectra corrected for propagation effects for shorter periods from 20 s to 1.0 s (e.g., Ye et al., 2016). The spectrum has a deep notch at the period of ~ 10 s and deviates significantly from a Brune ω^{-2} spectrum with the same seismic moment and a stress parameter of 3 MPa. We estimate the radiated energy $E_R = 5.49 \times 10^{14}$ J, with a moment-scaled radiated energy E_R/M_0 of 5.23×10^{-5} (Fig. 3b). As a continental intraplate rupture, the moment-scaled value is higher than the average value for large megathrust ruptures ($\sim 1.1 \times 10^{-5}$, Ye et al., 2016), as typically observed. It is significantly higher than that for the 2021 M_W 6.0 Yangbi mainshock (1.50×10^{-5}), which occurred on a relatively immature fault along the southwestern boundary of the Sichuan-Yunnan block (Gong et al., 2022). Overall, the relatively high E_R/M_0 and rupture velocity ($V_r \sim 2.8$ km/s) for the 2022 M_W 6.6 Luding earthquake, compared to the 2021 M_W 6.0 Yangbi earthquake ($E_R/M_0 = 1.50 \times 10^{-5}$ and $V_r \sim 2.0$ km/s from Gong et al., 2022) and the 2019 M_W 7.4 Ridgecrest earthquake ($E_R/M_0 = 1.4 \times 10^{-5}$ and $V_r \sim 1.5$ km/s from Liu et al., 2019), imply that it has ruptured a relatively mature fault.

3. The aftershock sequence

3.1. Spatial clustering of aftershocks and focal mechanisms

The 2022 M_W 6.6 Luding earthquake has extensive aftershocks, distributed in distinct zones along the Moxi segment, conjugate subfaults, and at the eastern flank of Mt. Gongga (Fig. 6). We classify aftershocks in four zones. Zone I is for aftershocks on and near the Moxi segment, from the epicenter to the southeast over 35 km. Aftershocks in Zone II occurred on a subfault in the northwest of the mainshock with a slightly different strike from the Moxi segment. Aftershocks in Zone III, located east of Mt. Gongga, appeared to occur on structures distinct from

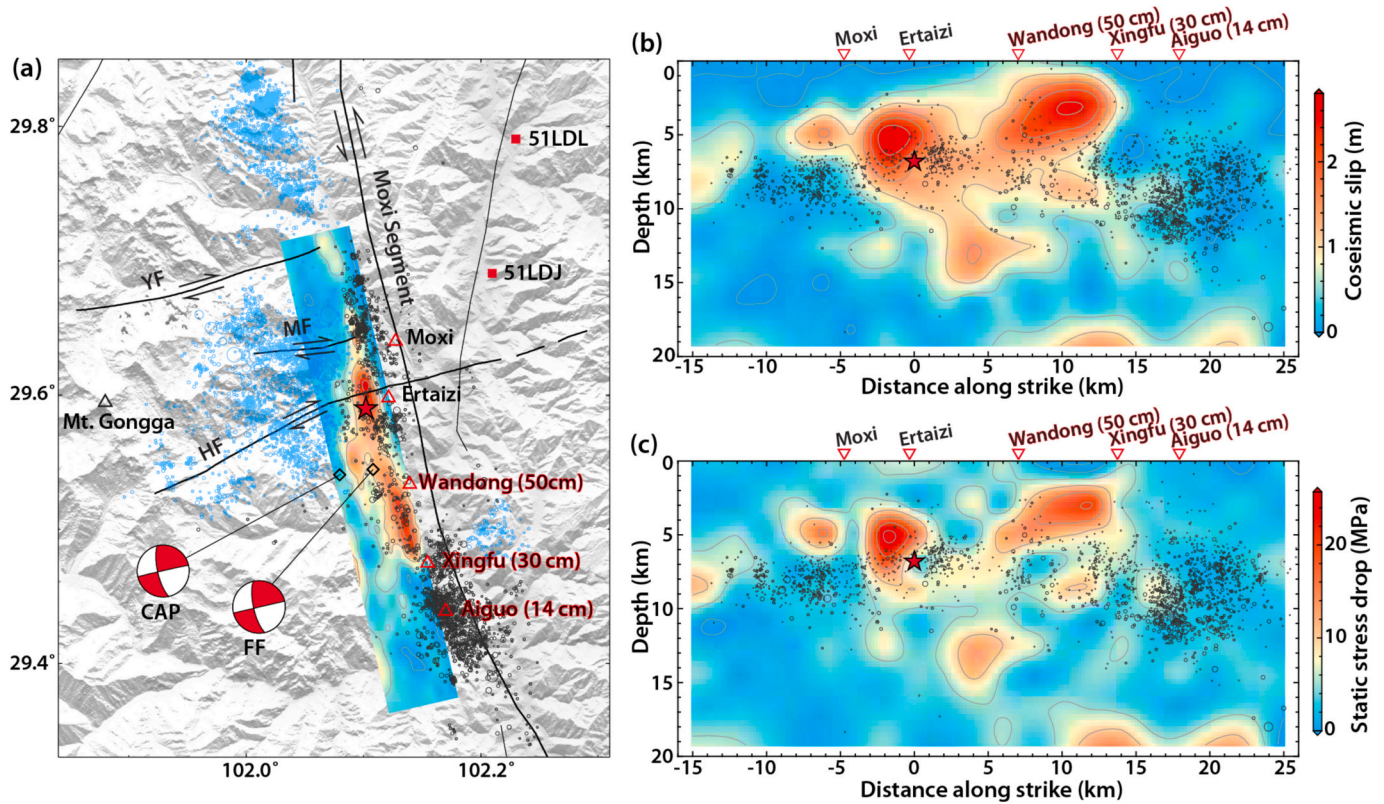


Fig. 5. Spatial correlation between our preferred mainshock slip model and the 15-day aftershocks. The 15-day aftershocks from 5 to 20 September 2022 are taken from the high-resolution catalog by Zhao et al. (2023) and plotted as black circles for events along the Xianshuihe fault and cyan circles for others. The surface breaks of 50 cm, 30 cm, and 14 cm are observed at Wandong, Xingfu, and Aiguo villages, respectively (Li et al., 2023). (a) Map view of projected coseismic slip, aftershocks, and nearby faults. YF: Yangzigou fault; MF: Mozigou fault; HF: Hailougou fault. The data for Yangzigou, Mozigou, and Hailougou faults are from Feng et al. (2018). The centroid locations of our slip model and the CAP inversion are marked by diamonds with corresponding focal mechanisms. (b-c) Depth view of coseismic slip and static stress drop with on-fault aftershocks. Gray contours in (b) and (c) indicate the coseismic slip in 0.5-m intervals and the stress drop in 5-MPa intervals, respectively. (For interpretation of the references to colour in this figure legend, the reader is referred to the web version of this article.)

the Moxi segment. Aftershocks in Zone IV occurred on a subfault near the southeastern end of the mainshock rupture, intersecting with the Moxi segment at roughly a right angle. Compared to the low seismicity and few M3.0+ aftershocks on the Moxi segment and its subfaults after the first 3 months, there were numerous aftershocks including several M3.0+ events still at the eastern flank of Mt. Gongga in nine months (Fig. 6). On 26 January and 28 February 2023, M_S 5.5 and M_S 4.8 earthquakes occurred, respectively, followed by a series of M3.0+ earthquakes (Fig. 6f).

To investigate the corresponding activated faults in each aftershock zone, we perform the point-source focal inversion for large aftershocks with M3.0+ using regional broadband seismic waveform data from ChinArray (Fig. 7c). As of 1 March 2023, 34 M3.0+ aftershocks are reported by CENC, and 28 of 34 have regional broadband seismic waveform data with a good signal-to-noise ratio. We invert for focal mechanism and centroid depth of 28 aftershocks with the regional broadband waveforms within 400 km using the CAP method. P and S waveforms are bandpass filtered at 0.02-0.15 Hz and 0.02-0.10 Hz for relatively large aftershocks, same as that for the mainshock, and at 0.03-0.20 Hz and 0.03-0.10 Hz for small aftershocks. The inversion results are listed in Table 2 and Figs. A7-A9. The focal mechanism and centroid depth of earthquakes in four aftershock zones are distinct (Fig. 7). In Zone I along the Moxi segment, 4 aftershocks are left-lateral strike-slip at centroid depths of 4.08.0 km, and one is a thrust event at 11.0 km. On the northwest subfault (Zone II), two aftershocks have almost identical left-lateral strike-slip mechanisms at 5.5 km with strikes following the seismicity trend, deviating from that of the Moxi segment. In the southeast subfault (Zone IV), two aftershocks have significant thrust

components at deeper centroid depths of 9.5 km and 11.0 km. All aftershocks at the eastern flank of Mt. Gongga (Zone III) have normal-faulting mechanisms, with the northwest-southeast strike roughly parallel to the Moxi segment. They have relatively shallower centroid depths of 3.0-7.0 km. We estimate the b value of aftershocks from 5 September 2022 to 1 June 2023 using the CENC catalog. The slightly lower b values for aftershocks on the Moxi segment (0.91) and at the eastern flank of Mt. Gongga (0.93) than that for the northwest subfault (Zone II; $b = 1.11$) (Fig. A10) indicate more well-developed faulting structures along the Moxi segment and underneath the eastern flank of Mt. Gongga than along the northwest subfault.

3.2. Static Coulomb stress changes in aftershock zones

Coulomb failure stress change (ΔCFS) induced by the mainshock rupture has proved to be an effective approach to evaluate if it promotes or inhibits the occurrence of earthquakes on nearby faults as aftershocks (King et al., 1994; Toda and Stein, 2022). To understand the aftershock distribution of the 2022 Luding sequence, we calculate the static ΔCFS imparted by the mainshock using the Coulomb 3.3 software (Toda et al., 2011) with our preferred coseismic slip model. We adopt the typical values of 0.4, 0.25, and 80 GPa as the coefficient of friction, Poisson's ratio, and Young's modulus, respectively.

The alignment of aftershock clusters and focal mechanisms of large aftershocks in each zone are used to help determine the receiver fault plane for calculating ΔCFS , and we show the ΔCFS at centroid depths for large aftershocks (Fig. 8). In Zone I along the Moxi segment, we calculate the Coulomb stress change at 7.0 km for the receiver fault plane of

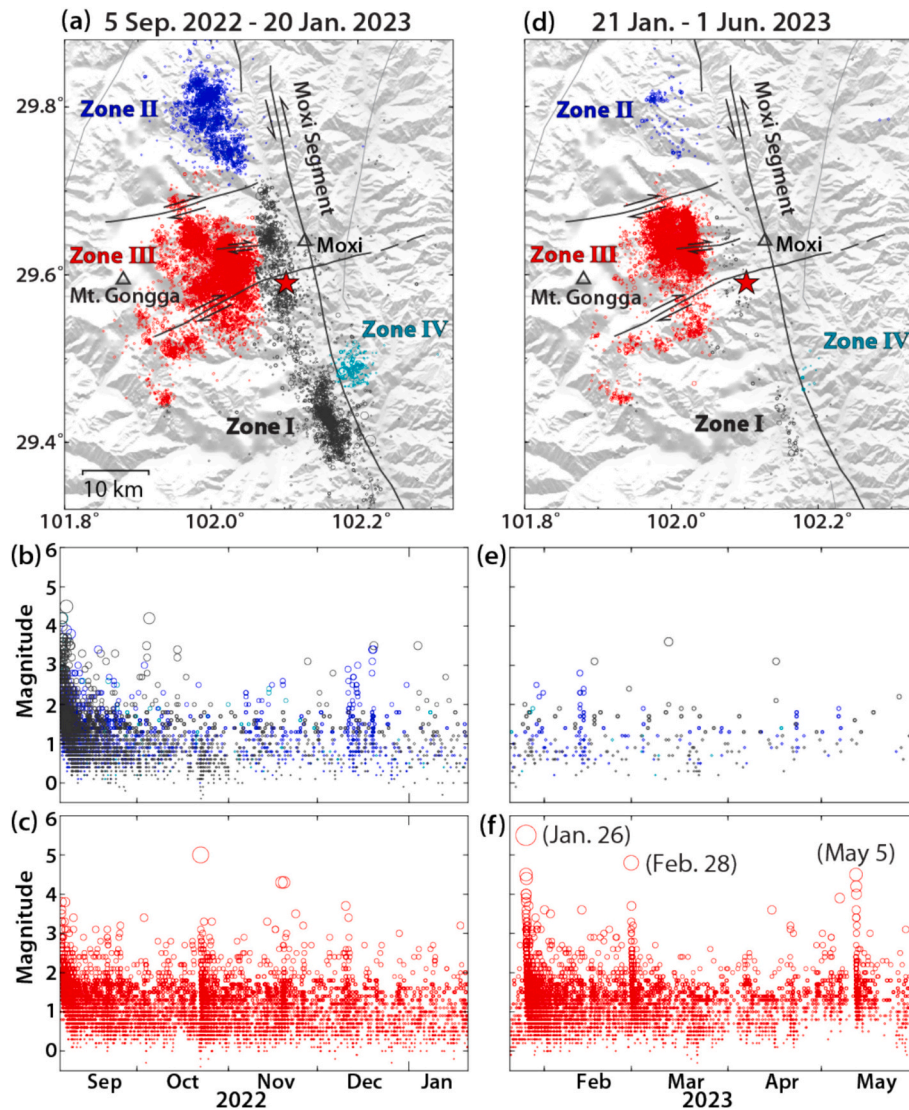


Fig. 6. Spatial and temporal variation of aftershock seismicity during (a-c) 5 September 2022 to 20 January 2023 and (d-f) 21 January to 1 June 2023. Earthquake information is from the CENC catalog. The red star indicates the 2022 Luding mainshock on 5 September 2022. Black, blue, red, and cyan dots show seismicity in Zone I at the Moxi segment along the Xianshuihe fault, Zone II on a subfault to the NWN, Zone III at east of Mt. Gongga to the west of Moxi, and Zone IV on a subfault nearly perpendicular to the Moxi segment. The temporal evolution of seismicity at different zones is illustrated in the two panels below. (For interpretation of the references to colour in this figure legend, the reader is referred to the web version of this article.)

strike=331°, dip=74°, and rake=-1°. Most aftershocks are distributed in the southernmost parts with positive Δ CFS larger than 0.4 MPa, while some aftershocks distributed near the mainshock rupture area with negative Δ CFS. In Zone II on the northwest subfault, the Δ CFS on the receiver fault (strike=324°, dip=85°, rake=-11°) at depth of 5.5 km are mostly positive more than 0.1 MPa. In Zone III at the eastern flank of Mt. Gongga, we set the receiver fault plane with strike=161°, dip=63°, and rake=-101°, based on the aftershock focal mechanism. Most aftershocks, especially all M3.0+ aftershocks, are distributed in the region with positive Δ CFS at depth of 7.0 km more than 0.4 MPa, with only few aftershocks distributed in the southeastern part with negative Δ CFS. We get a similar pattern of Δ CFS (Fig. 8c) with two different receiver fault planes, given by the focal mechanism of another aftershock and the other nodal plane of the largest aftershock (Fig. A11). In Zone IV on the southeast subfault, the Δ CFS on the receiver fault (strike=69°, dip=56°, rake=148°) at depth of 9.5 km have minor negative or positive values less than 0.1 MPa. The uncertainties of the receiver-fault plane, the simplified coseismic model (Dieterich and Smith, 2009), and dynamic stress triggering (Hardebeck and Harris, 2022) may account for the

discrepancy between aftershock distribution and the computed static Δ CFS. Nonetheless, given the overall positive static Δ CFS in most aftershock areas, we conclude that the static stress transfer from the mainshock rupture has made a significant contribution in promoting the occurrence of aftershocks.

4. Discussion

4.1. Seismic potential in the Moxi segment along the Xianshuihe fault

The accumulated stress on a fault due to the relative motion of bounding blocks on both sides of the fault is commonly released by earthquake rupture or creep. With the earthquake catalog with a complete magnitude larger than 6.5 in the last three centuries on the Xianshuihe fault (Li et al., 2021), we evaluate the relative slip budget in the Moxi segment. Wen et al. (2008) refined the positions and spatial extents of 18 M6.0+ historical earthquakes on the Xianshuihe fault from 1700 to 1981 based on the distributions of damage, surface ruptures, and aftershocks of historical and modern earthquakes. We apply the empirical

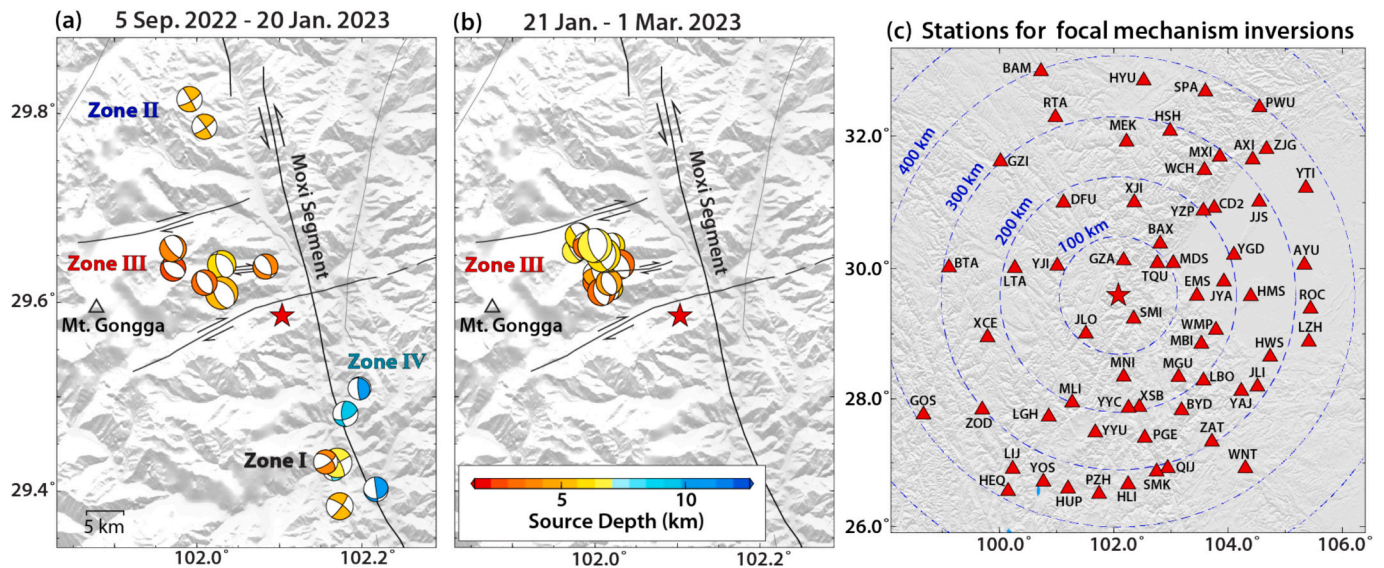


Fig. 7. Focal mechanisms for M_L 3.0+ aftershocks inverted with regional data using the CAP method. (a) Spatial distribution of the focal mechanisms from 5 September 2022 to 20 January 2023 (E01 - E15 in Table 2). (b) Spatial distribution of the focal mechanisms from 21 January to 1 March 2023 (E16 - E28 in Table 2). (c) Regional broadband seismic stations for the CAP inversion of focal mechanisms.

Table 2

Focal mechanism information for the 2022 aftershock sequence (E01-E28) and the 2016 sequence (E1a-E4a).

ID	Origin time (UTC+8)	Lon	Lat	H (km)	M_L	Strike	Dip	Rake	M_W
E01	2022-09-05 17:39:21	102.173°	29.384°	5.0	4.0	304°	75°	-10°	4.26
E02	2022-09-05 18:31:19	102.156°	29.431°	4.0	3.7	310°	52°	-25°	3.82
E03	2022-09-05 19:26:20	102.180°	29.482°	9.5	4.2	69°	56°	148°	3.99
E04	2022-09-06 05:28:41	102.083°	29.638°	4.0	3.7	339°	56°	-64°	3.96
E05	2022-09-06 17:54:47	102.009°	29.621°	3.0	3.8	330°	44°	-90°	4.04
E06	2022-09-07 02:42:15	102.170°	29.430°	7.0	4.5	331°	74°	-1°	4.65
E07	2022-09-07 05:39:56	101.991°	29.815°	5.5	3.9	329°	87°	-16°	4.01
E08	2022-09-07 08:34:35	102.197°	29.509°	11.0	3.7	315°	14°	50°	3.61
E09	2022-09-07 09:46:21	102.166°	29.423°	8.0	3.7	290°	53°	21°	3.55
E10	2022-09-08 15:12:02	102.009°	29.786°	5.5	3.8	324°	85°	-11°	3.97
E11	2022-10-05 03:17:26	102.217°	29.402°	11.0	4.2	172°	90°	66°	3.89
E12	2022-10-22 13:17:01	102.030°	29.610°	5.0	5.0	159°	53°	-73°	5.13
E13	2022-11-18 21:23:56	102.030°	29.640°	6.0	4.3	165°	59°	-69°	4.47
E14	2022-11-19 18:28:49	101.971°	29.657°	4.0	4.3	139°	71°	-107°	4.22
E15	2022-12-10 15:09:17	101.971°	29.636°	2.5	3.7	134°	43°	-73°	4.01
E16	2023-01-26 03:49:43	102.000°	29.660°	7.0	5.5	161°	63°	-101°	5.39
E17	2023-01-26 03:50:16	102.010°	29.650°	6.0	4.5	160°	65°	-101°	5.40
E18	2023-01-26 04:30:43	102.017°	29.621°	4.5	3.9	165°	42°	-80°	4.09
E19	2023-01-26 04:51:09	102.008°	29.611°	3.5	4.0	165°	43°	-85°	4.39
E20	2023-01-26 04:57:18	101.990°	29.660°	3.5	4.0	165°	64°	-56°	4.31
E21	2023-01-26 05:19:07	101.980°	29.670°	6.0	3.3	141°	78°	-99°	4.17
E22	2023-01-26 05:22:11	101.975°	29.654°	6.5	3.6	147°	73°	-99°	3.78
E23	2023-01-26 07:21:32	102.030°	29.640°	3.5	4.4	156°	46°	-81°	4.67
E24	2023-01-27 01:11:03	102.001°	29.630°	4.5	3.7	160°	70°	-42°	3.98
E25	2023-02-01 02:59:31	102.019°	29.615°	6.0	3.6	163°	55°	-84°	3.83
E26	2023-02-13 01:23:35	102.021°	29.660°	6.0	3.6	161°	55°	-105°	3.94
E27	2023-02-28 22:46:50	102.010°	29.630°	6.5	4.8	158°	61°	-90°	5.01
E28	2023-03-01 00:49:57	102.001°	29.622°	3.0	3.7	155°	43°	-94°	4.08
E1a	2016-03-18 01:19:53	102.002°	29.604°	2.5	4.4	161°	51°	-56°	4.39
E2a	2016-03-21 11:35:49	101.997°	29.619°	1.5	4.0	161°	36°	-35°	4.27
E3a	2016-03-24 01:55:38	102.016°	29.607°	2.5	4.2	339°	84°	45°	4.32
E4a	2016-03-25 06:03:52	101.984°	29.609°	3.5	3.9	149°	49°	-78°	4.02

relationship between rupture length and seismic moment (Shimazaki, 1986) to estimate the spatial extents of the 1893 M6.0 and 1911 M6.3 earthquakes which are not listed in Wen et al. (2008). We adopt the slip model for the 2014 M6.4 Kangding earthquake from Zhang et al. (2021). Historical earthquake sequence exhibits a distinct boundary in time around the year 1816. Before 1816, the whole Xianshuihe fault had ruptured since 1700, and after 1816 there was a 77-year period of seismic quiescence until the occurrence of the 1893 M7.0 earthquake. It appears that a new cycle started since the 1816 M7.5 earthquake, so we

calculate the accumulated seismic moment since 1816 (Fig. 2b). Except for the Moxi segment, there have been M6.0+ earthquakes along the Xianshuihe fault. There remained a seismic gap in the Moxi segment, so the occurrence of the 2022 M_W 6.6 Luding earthquake is not surprising.

Considering that 1327 M7.5 and 1786 M7.8 earthquakes ever ruptured the entire Moxi segment with similar positions and spatial extents of ~ 90 km, we can estimate a rate of seismic moment deficit of $0.53\text{--}1.51 \times 10^{16}$ Nm/(a-km) based on the 459-year period and the accumulated seismic moment of $2.21\text{--}6.24 \times 10^{20}$ Nm (M_W 7.5–7.8). The

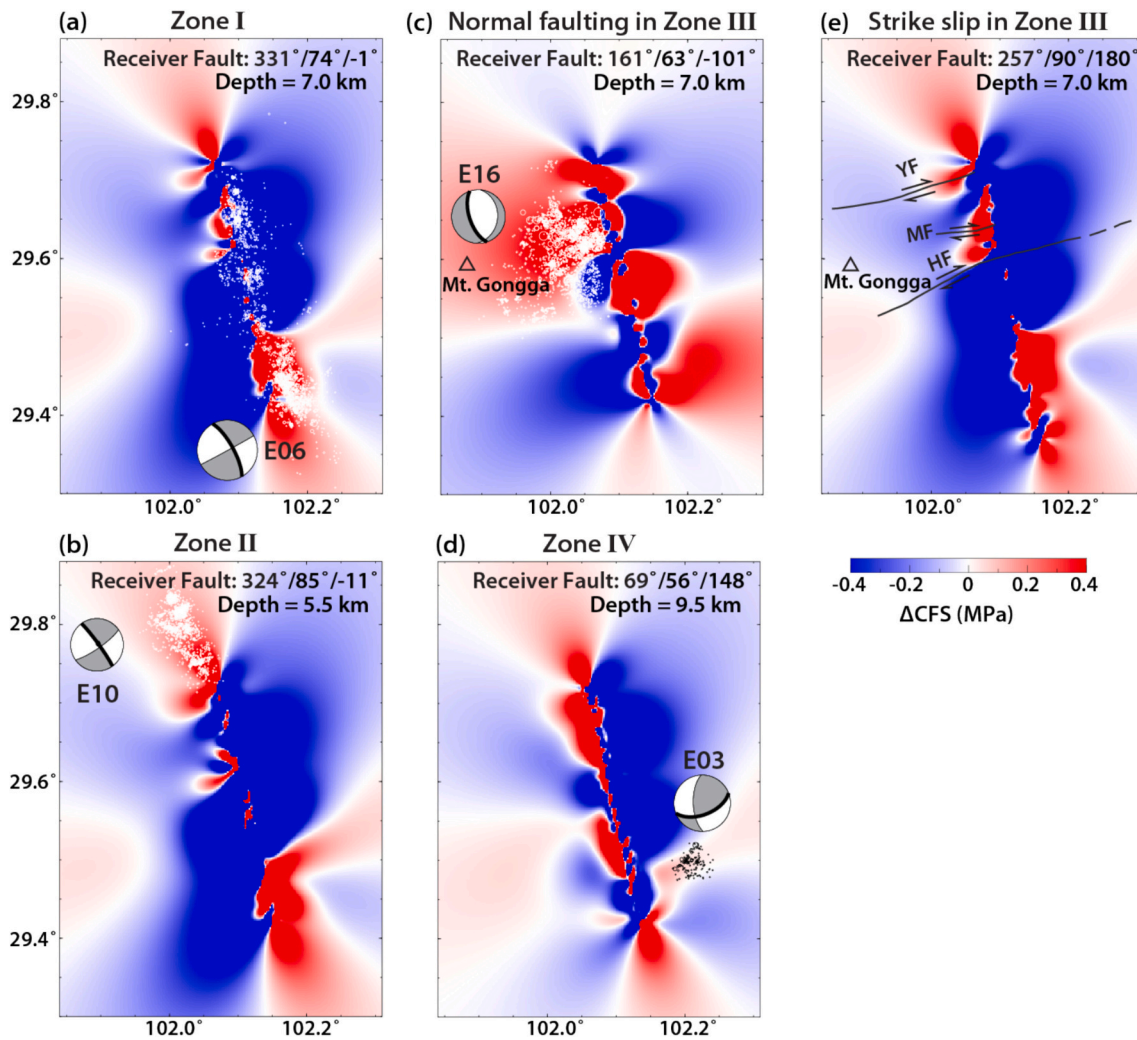


Fig. 8. Static Coulomb failure stress changes (ΔCFS) in aftershock zones. Small circles indicate the aftershocks from the high-resolution aftershock catalog by Zhao et al. (2023). (a-d) The ΔCFS are calculated at receiver faults with one nodal plane of the largest aftershock at its optimal centroid depth (E06, E10, E16, and E03 in Table 2). (e) The receiver fault is a vertical strike-slip fault with the strike of 257° , similar to YF, MF and HF.

seismic moment deficit is about $2.50\text{--}7.13 \times 10^{19}$ Nm (M_w 6.9–7.2) over the 20-km-long rupture area for the 2022 Luding earthquake since 1786, and it is about balanced for the southern part of the Moxi segment. However, no large earthquakes have ruptured the northern part of the Moxi segment since 1786, showing the aperiodicity and segmentation of rupture behaviors in this section, possibly due to the complex fault geometry associated with bends, junctions and branches. The 1955 M7.5 Kangding earthquake likely occurred on the whole Zheduotang fault, a branch fault in the Bamei-Kangding segment along the Xianshuihe fault to the north, and stopped the northernmost part of the Moxi segment, based on the distribution of aftershocks and surface rupture (Allen et al., 1991; Li et al., 1997). There could be significant accumulated seismic moment in the northern part of the Bamei-Kangding segment with only the 2014 M6.4 Kangding earthquake over the last 238 years (Fig. 2b). Jiang et al. (2015) get the interseismic coupling at the northern part of the Bamei-Kangding segment up to 60%. However, Li et al. (2021) recognize it as a creeping fault with small interseismic coupling (less than 20%). Given the relatively high seismicity in the past several decades, we can rule out the possibility of a large earthquake in the northern part of the Bamei-Kangding segment, and the seismic hazard would be severe if it ruptures together with the north section of the Moxi segment.

We calculate the static ΔCFS imparted by the 2022 M_w 6.6 Luding mainshock on the unruptured Moxi segment and other surrounding

faults (Fig. 9). Variable receiver planes are set up for different faults at the receiver depth of 10 km. The receiver plane of the Moxi segment is determined from the focal mechanism of the 2022 Luding mainshock. The receiver planes for other faults are associated with vertical left-lateral strike-slip faulting from Li et al. (2022), except for the reverse-faulting Longmenshan fault. The results show that the ΔCFS are negative in the southern Moxi segment and positive in the north (Fig. 9). The positive ΔCFS on the northern Moxi segment (Moxi-Kangding segment) is large, up to 0.1 MPa, indicating that the 2022 Luding mainshock promotes the rupture on it. The positive ΔCFS of less than 0.03 MPa on the Kangding-Bamei segment of the Xianshuihe fault and 0.04 MPa on the Longmenshan fault indicate that the mainshock may slightly promote the rupture on them. The ΔCFS on the Xiaojinhe, Anninghe, and Daliangshan faults are less than 0.02 MPa, suggesting mild effect from the 2022 Luding earthquake.

4.2. Mechanism of normal faulting underneath the eastern flank of Mt. Gongga

One interesting feature of the 2022 Luding earthquake sequence is the normal-faulting aftershock activity underneath the eastern flank of Mt. Gongga (west of the mainshock), which persisted intermittently for 9 months (Fig. 6). The three E-W trending, right-lateral strike-slip sub-faults (Yanzigou fault, Mozigou fault, and Hailougou fault), near the

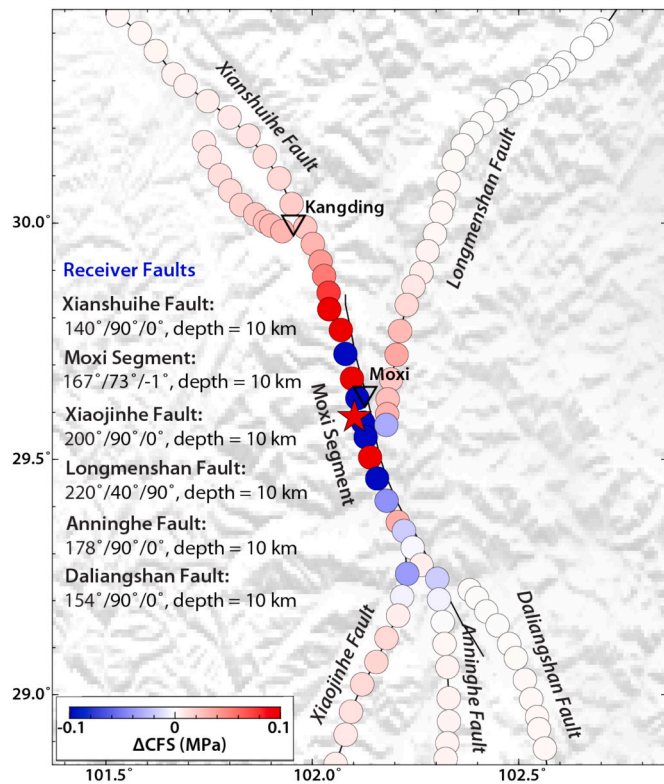


Fig. 9. Static Coulomb failure stress changes (ΔCFS) on the Moxi segment and nearby faults from the 2022 M_w 6.6 Luding earthquake. The receiver fault orientations are from Li et al. (2022). The ΔCFS is calculated at depth of 10 km. The red star indicates the epicenter of the mainshock. (For interpretation of the references to colour in this figure legend, the reader is referred to the web version of this article.)

eastern flank of Mt. Gongga (Fig. 5a), seem not activated as $M3.0+$ aftershocks which are dominantly NW-SE trending normal faulting. The seismicity in the east of Mt. Gongga significantly increased with the

impoundment of the nearby Dagangshan reservoir in 2015–2016 (Fig. 10). Using the amplitude ratios of direct P and S waves, Feng et al. (2018) find dominant right-lateral strike-slip focal mechanisms for large events in the 2016 sequence and infer that they occurred on the NEE-SWW trending strike-slip Mozigou fault. We invert the focal mechanisms of four $M3.0+$ earthquakes in the 2016 sequence using regional waveform data with the CAP method, and find that one M_w 4.32 event (E3a) has a strike-slip focal mechanism while three others are dominated by normal faulting with shallower centroid depths of ~ 3.0 km, similar to the focal mechanisms of aftershocks in the 2022–2023 sequence (Fig. 10). The handpicked polarities of P waves confirm our results (Fig. A12). It suggests that most seismicity at the eastern flank of Mt. Gongga might be all controlled by some pre-existing structures for the shallow normal faulting, and we propose an unmapped NW-SE trending extensional fault system, about parallel to the Moxi segment along the Xianshuihe fault (Fig. 11).

The Coulomb wedge theory (Wang and Hu, 2006) suggests that a high mountain with a steep slope tends to collapse under its own weight, thus having the potential to create internal tensional deformation such as normal faults. Once created, these normal faults can be reactivated by the episodic occurrence of basal weakening (Cubas et al., 2013) or basal erosion (Wang et al., 2010). We infer that this may be the case for the Mt. Gongga region, where the steep slope along the eastern flank of the mountain, with a dramatic elevation change over 5000 m within a range of 20 km, can favor the development of NW-SE trending normal faults beneath the mountain (F1 in Fig. 11). We calculate the theoretical critical envelope for a wedge based on the available information of Mt. Gongga to further interpret these normal faults. We aim to reconstruct the conditions required for developing normal faults at certain stage of Mt. Gongga's geological past, while also remarking that the calculation is based on quasi-static stress balance without considering material/structural heterogeneities or thermal anomalies. The mean topographic slope (α) of the wedge above the aftershock zone in eastern Mt. Gongga (along the profile W-E in Fig. 11a) is estimated as 14.3° (Fig. 11b). According to the 3D resistivity model of Jiang et al. (2022) beneath the eastern Mt. Gongga, there is a westward dipping resistive body at the middle crust that is interpreted as the underthrusting of the Yangtze Craton. We regard the upper boundary of the westward dipping resistive

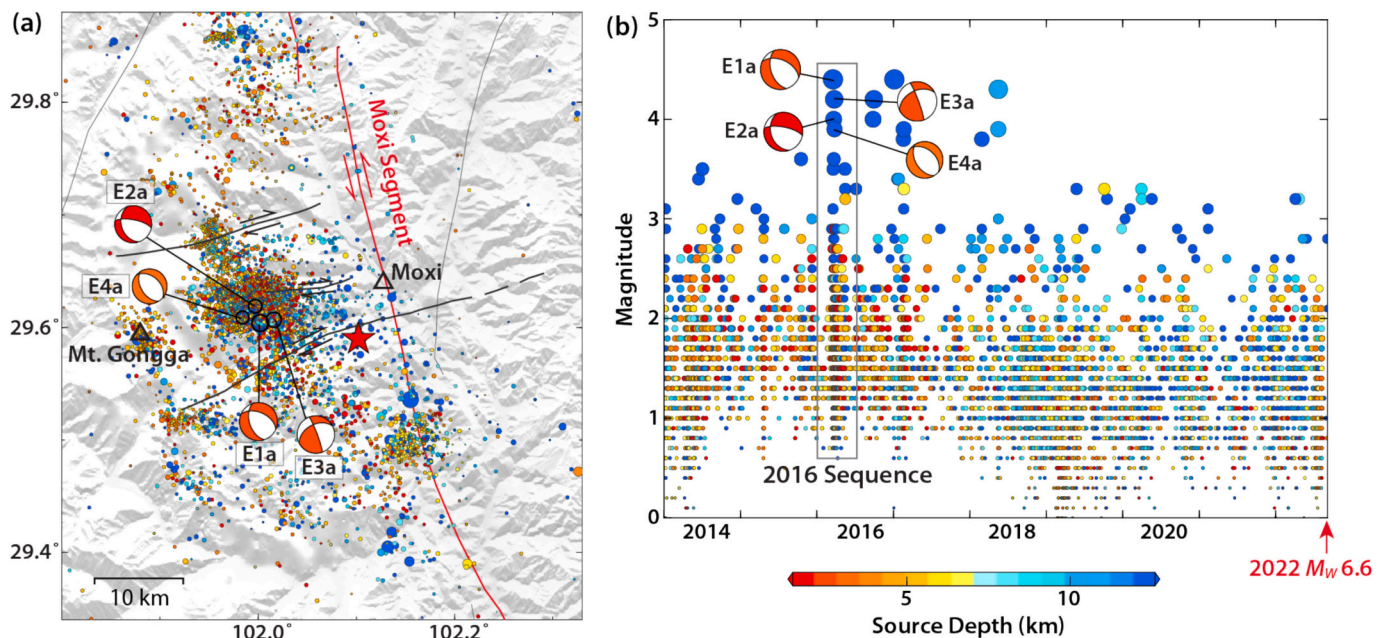


Fig. 10. Spatial and temporal variation of background seismicity from 2014 to 5 September 2022. Earthquake information is from the CENC catalog. The red star indicates the 2022 Luding mainshock on 5 September 2022. The 2016 sequence is highlighted by the gray box in (b) with the focal mechanisms for the 4 largest events (E1a–E4a in Table 2). (For interpretation of the references to colour in this figure legend, the reader is referred to the web version of this article.)

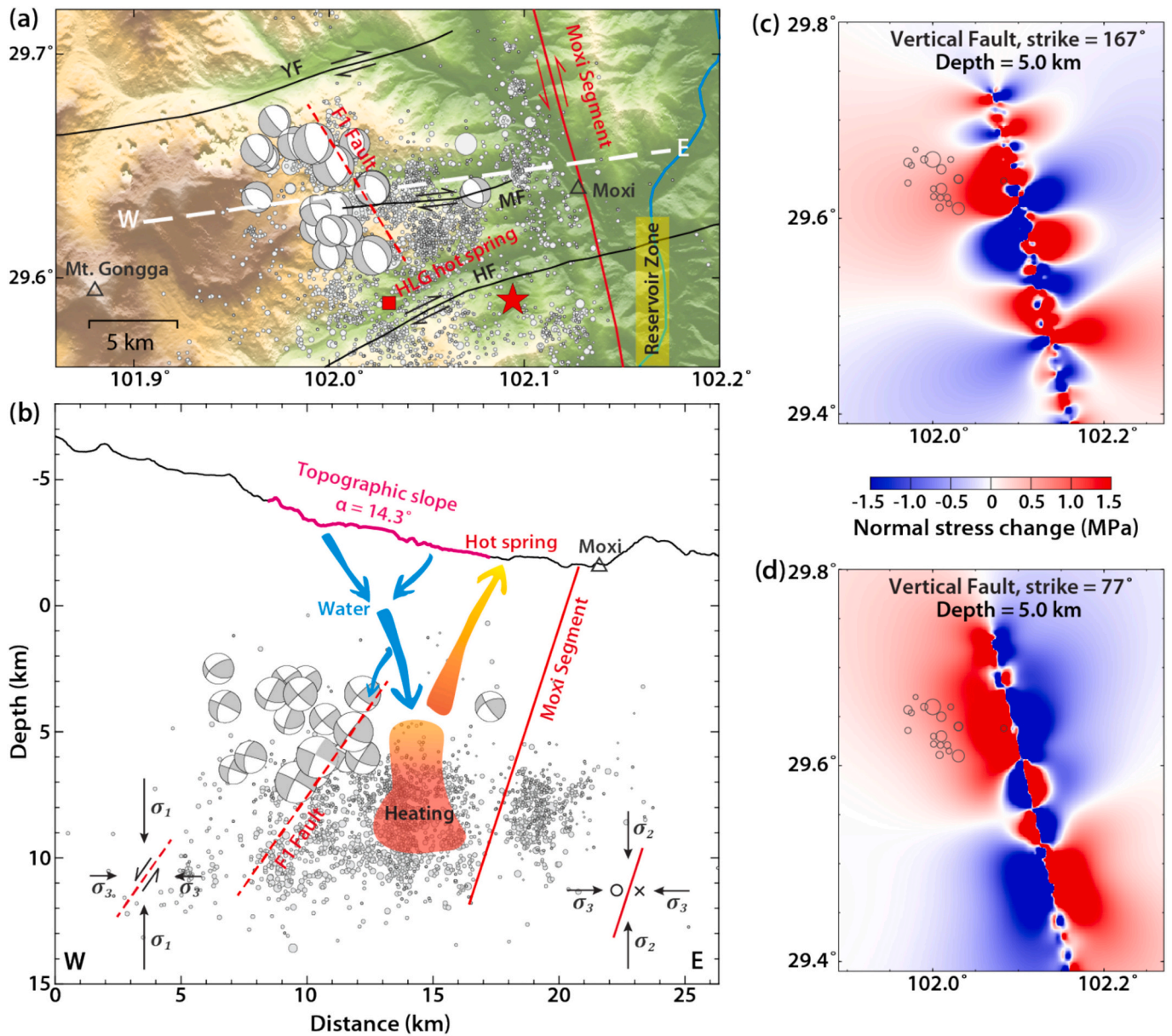


Fig. 11. Geological setting and fault structures near the eastern Mt. Gongga. (a) Spatial distribution of the 2022 aftershock sequence from 5 to 20 September (Zhao et al., 2023), along with the major faults. The red diamond shows the location of the HLG hot spring (Yuan et al., 2015). F1 Fault indicates the inferred NW-SE trending weak normal fault underneath the eastern flank of Mt. Gongga from the focal mechanisms. According to the coherence of the nodal plane solutions, we assume the normal fault is dipping to the west (F1). The vertical cross-section W-E is shown in (b) with aftershocks only within 5 km away. $\alpha = 14.3^\circ$ indicates the mean topographic slope above the western aftershock zone. Paired arrows at the bottom left and bottom right indicate the likely stress regime underneath eastern Mt. Gongga and along Luding mainshock rupture zone, respectively, with σ_1 , σ_2 , and σ_3 denoting maximum, intermediate, and minimum principal stress. Due to the horizontal tensional stress changes impacted by the Luding mainshock (see results in (c) and (d)), the stress regime underneath eastern Mt. Gongga is favorable for normal faulting. (c) and (d) Normal stress changes at 5 km depth induced by the mainshock on two vertical faults with strike = 167° (NW-SE) and strike = 77° (NE-SW) directions, respectively. Gray circles show the large normal-faulting aftershocks. (For interpretation of the references to colour in this figure legend, the reader is referred to the web version of this article.)

body as a basal décollement and estimate the dip (β) of the wedge as 30.0° . Besides α and β , there are four other model parameters: the internal coefficient of friction and pore fluid pressure ratio within the wedge, and the corresponding ones on the basal décollement. We get the critical envelope (the upper and lower branch for extensional and compressional failure, respectively) for different sets of model parameters (Fig. A13). The results show that the wedge with a steep slope (α) tends to create extensional failure (i.e., toward the upper branch of the envelope), and the wedge structure in eastern Mt. Gongga may be a response to a high pore fluid pressure ratio and/or low basal coefficient of friction. We note that in general the Coulomb wedge theory, upon

reaching a critical state, would predict conjugate splay faults within the wedge. However, in the actual situation, only one set of splay faults may prevail due to factors such as material/structural heterogeneities. According to the coherence of the nodal plane solutions, we assume the normal faults are dipping to the west (Fig. 11b).

While the above argument explains the initial development of normal faults, these faults and hence the wedge may subsequently show a switch between stable and unstable states, depending on the evolutions of stress, friction, pore fluid pressure, and other parameters (Wang and Hu, 2006). Apparently, the eastern Mt. Gongga region was at a relatively stable state right before the 2022 Luding mainshock, while it

has entered an unstable state afterwards due to the tensional stress change induced by the 2022 Luding mainshock. Considerable tensional stress change by the 2022 Luding mainshock is expected to be along the NW-SE direction (Fig. 11d), and some tensional stress change can also be produced along the NE-SW direction as well (Fig. 11c). This can cause both the horizontal principal stresses and the pore fluid pressure to decrease. However, the net effect should be to reduce the effective normal stress and hence strength along the considered normal faults, thus promoting their reactivation. Due to the aforementioned stress changes impacted by the Luding mainshock, the N-S compressional stress becomes intermediate while the W-E compressional stress becomes even smaller in the aftershock zone beneath the eastern Mt. Gongga (Fig. 11b).

Earthquake activity under stress perturbations can be used to infer the criticality and strength of faults (Beroza and Zoback, 1993; Hardebeck and Okada, 2018). Specifically, it has been suggested that close-to-failure and weak faults are more likely to host triggered seismicity under slight stress perturbations (Houston, 2015). Here, the impoundment of the Dagangshan reservoir or the stress transfer from nearby earthquakes may trigger seismicity in the area around Mt. Gongga. For the 2015–2016 sequence triggered by the Dagangshan reservoir, most of the events occurred in the east of Mt. Gongga rather than on the Moxi segment closest to the reservoir (Fig. 10), indicating that the faults underneath the eastern flank of Mt. Gongga may be more susceptible to small stress perturbations (therefore weak). Similar indications can also be found from the 2022 Luding earthquake sequence, where the area in the east of Mt. Gongga (Zone III) hosted shallower aftershocks with long-lasting higher seismicity (implying lower differential stress) than those on the Moxi segment (Fig. 6). Moreover, several hot springs reported in the east of Mt. Gongga, such as the well-known Hailuogou hot spring with a high temperature of $\sim 90^\circ\text{C}$, may support the existence of weak faults underneath the eastern flank of Mt. Gongga. According to Yuan et al. (2015), there are well-developed structural fissures through which atmospheric precipitation and snow-melting water can penetrate into deep faults. Then, the water will be heated and transported to the surface in the fault fracture zone to form hot springs. The abundant water entering the faults increases the pore fluid pressure to weaken the faults (Fig. 11b).

Elevated temperature in the crust and presence of abundant fluid in the Mt. Gongga region has also been suggested by other studies. According to Cook et al. (2018), hot weak rocks and focused precipitation, among other factors, contribute to the rapid uplift and exceptional topography of Mt. Gongga. Zircon U-Pb ages of samples collected throughout the Gongga granite range from 30 Ma to 5 Ma (Li and Zhang, 2013; Searle et al., 2016), which implies that crustal melting occurred during much of the Cenozoic and may still be in progress. The current monsoon system in China was established at ~ 23 Ma (Sun and Wang, 2005; Clift et al., 2008), and an orographic barrier was possibly formed by at least 10 Ma, leading to high and focused precipitation in the Mt. Gongga region. Downward flow of surface-derived fluid deep into the crust can be facilitated by a high topography above the fault, a coseismic increase of permeability in the fault zone at depth, and a slow post-seismic healing/sealing (Sibson, 1994; Ingebritsen and Manning, 2010; Ague, 2014; Miller, 2020; Bock et al., 2024; Simpson, 2024), which may be the case for the Mt. Gongga region (recalling that it is located in the tensional quadrant of the 2022 Luding mainshock). According to the 3D resistivity model of Jiang et al. (2022), there is a westward dipping resistive body at the middle crust beneath the eastern Mt. Gongga, overlaid with a thin, sub-horizontal low-resistivity layer, potentially indicative of the presence of partial melt or fluid. This low resistivity layer may also facilitate the heating of the fluid penetrating from the surface and contribute to fault weakening. These evidences support an interplay among topography, surface-derived fluid (due to snow melting and precipitation), hot crustal rocks, hot springs, nearby tectonic (or non-tectonic) activity, and normal-faulting seismicity in the eastern Mt. Gongga (Fig. 11b).

Combining all of the above, we suggest that there exist NW-SE trending normal faults underneath the eastern flank of Mt. Gongga, which were previously developed due to the gravitational collapse of Mt. Gongga. These normal faults are weak due to their shallow depth and environment-related pore fluid pressure. After the 2022 Luding mainshock, these pre-existing weak fault planes become reactivated to host NW-SE trending normal-faulting aftershocks and remain in a fragile state for 9 months, longer than in other aftershock zones.

5. Conclusion

Combining teleseismic data and regional GNSS static deformation, we find that the 2022 M_W 6.6 Luding earthquake has an asymmetrical rupture along the strike extending southeastward by ~ 15 km with a peak slip of ~ 2.8 m and northwestward by ~ 5 km with minor slip, with two main slip patches near the hypocenter and at a shallower area ~ 10 km to the southeast, respectively. Our slip model shows that the SE rupture reaches the surface, consistent with the field observation. The rupture at the southern part of the Moxi segment approximately balanced the slip deficit since the 1786 $M_7.8$ earthquake. The northern part of the Moxi segment has remained relatively silent and receives a positive ΔCFS of ~ 0.1 MPa from the 2022 mainshock, posing a high seismic potential. The aftershocks are mainly distributed in distinct zones. Compared to those along the Moxi segment or its subfaults with strike-slip focal mechanisms, aftershocks underneath the eastern flank of Mt. Gongga are dominated by normal faulting with shallower centroid depth and intense seismicity lasts over ~ 9 months. We attribute these distinct features to the pre-existing normal faults underneath the eastern flank of Mt. Gongga, which were initially developed by the gravitational collapses of Mt. Gongga, and subsequently weakened by environment-related pore fluid pressure as supported by the existence of hot springs and the high susceptibility to nearby tectonic or non-tectonic activity. Our study provides a comprehensive understanding of the rupture behaviors of the 2022 Luding earthquake sequence, which can shed lights on the seismic hazard assessment both on the Moxi segment and its subfaults, and the potential interaction between strike-slip fault and nearby mountain areas.

CRedit authorship contribution statement

Wenzheng Gong: Writing – review & editing, Writing – original draft, Methodology, Formal analysis. **Lingling Ye:** Writing – review & editing, Writing – original draft, Supervision, Project administration, Methodology, Funding acquisition, Formal analysis, Conceptualization. **Shiqing Xu:** Writing – review & editing, Writing – original draft, Supervision, Funding acquisition, Formal analysis, Conceptualization. **Yipei Tan:** Writing – review & editing, Investigation, Data curation. **Xiaofei Chen:** Writing – review & editing, Supervision, Conceptualization.

Declaration of competing interest

The authors declare that they have no known competing financial interests or personal relationships that could have appeared to influence the work reported in this paper.

Data Availability

Regional broadband waveform data for this study are provided by Data Management Center of China National Seismic Network at Institute of Geophysics, China Earthquake Administration (SEISDMC, doi:10.11998/SeisDmc/SN, <http://www.seisdmc.ac.cn>), China Earthquake Networks Center and SC, YN, CQ, GZ Seismic Networks, China Earthquake Administration. The continuous waveform data can be requested with a preauthorized account from the Data Management Center of China Seismic Network. Teleseismic data were downloaded through the

IRIS Wilber 3 system (<https://ds.iris.edu/wilber3/>) with stations from Global Seismographic Network (II: <https://doi.org/10.7914/SN/II>, IU: <https://doi.org/10.7914/SN/IU>) and International Federation of Digital Seismic Networks (FDSN; <https://doi.org/10.7914/SN/CN>, AK: <https://doi.org/10.7914/SN/AK>, CZ: <https://doi.org/10.7914/SN/CZ>, DK, G: <https://doi.org/10.18715/GEOSCOPE.G>, GE: <https://doi.org/10.14470/TR560404>, GR: <https://doi.org/10.25928/mbx6-hr74>, JP, KO: <https://doi.org/10.7914/SN/KO>, MN: <https://doi.org/10.13127/SD/fBBtDtd6q>). The earthquake information is based on the catalogs provided by the National Earthquake Data Center at China Earthquake Network Center (CENC-NEDC; <https://data.earthquake.cn/>) and the U.S. Geological Survey National Earthquake Information Center (USGS-NEIC; <https://earthquake.usgs.gov/earthquakes>). The Global Centroid Moment Tensor (GCMT) solution is from <https://www.globalcmt.org/CMTsearch.html>. The GNSS static displacement data are from Li et al. (2022). Active faults data are from National Earthquake Data Center (<https://data.earthquake.cn/>), supported by China Earthquake Disaster Prevention Center, Seismic Active Fault Survey Data Center (<https://www.activefault-datacenter.cn>).

Acknowledgments

We thank Yan Hu and Yingquan Sang for helpful discussions. The work was supported in part by National Key Research and Development Program of China 2021YFC3000700 and Guangdong Program 2021QN02G106 (S. X.), National Key Research and Development Program of China 2023YFF0803200 (L. Y.), and Tianjin Science and Technology Plan Project 22JCYBJC00100 (Y. T.). We thank National Earthquake Data Center at China Earthquake Network Center, China Earthquake Data Center, and the IRIS Data Management Center, which provide waveform data and active fault information. Acknowledge for the Coulomb Stress software (Coulomb 3.3, Toda et al., 2011) and GMT software (Wessel et al., 2019).

Appendix A. Supplementary data

Supplementary data to this article can be found online at <https://doi.org/10.1016/j.tecto.2024.230538>.

References

- Ague, J.J., 2014. Fluid flow in the deep crust. In: Holland, H.D., Turekian, K.K. (Eds.), *Treatise on Geochemistry*, 2nd edition vol. 4. Elsevier, Oxford, pp. 203–247.
- Allen, C.R., Zhuo, L.L., Hong, Q., Xue, Z.W., Hua, W.Z., Wei, S.H., 1991. Field study of a highly active fault zone: the Xianshuihe fault of southwestern China. *Geol. Soc. Am. Bull.* 103 (9), 1178–1199.
- An, Y., Wang, D., Ma, Q., Xu, Y., Li, Y., Zhang, Y., Wang, B., 2023. Preliminary report of the September 5, 2022 M_s 6.8 Luding earthquake, Sichuan, China. *Earthquake Res. Adv.* 3 (1), 100184.
- Bai, M., Chevalier, M.L., Pan, J., Replumaz, A., Leloup, P.H., Métouis, M., Li, H., 2018. Southeastward increase of the late Quaternary slip-rate of the Xianshuihe fault, eastern Tibet. *Geodynamic and seismic hazard implications. Earth Planet. Sci. Lett.* 485, 19–31.
- Bai, Q., Ni, S., Chu, R., Jia, Z., 2020. gCAPjoint, a software package for full moment tensor inversion of moderately strong earthquakes with local and teleseismic waveforms. *Seismol. Res. Lett.* 91(6), 3550–3562.
- Bai, M., Chevalier, M.L., Leloup, P.H., Li, H., Pan, J., Replumaz, A., Zhang, J., 2021. Spatial slip rate distribution along the SE Xianshuihe fault, eastern Tibet, and earthquake hazard assessment. *Tectonics* 40 (11) e2021TC006985.
- Beroza, G.C., Zoback, M.D., 1993. Mechanism diversity of the Loma Prieta aftershocks and the mechanics of mainshock-aftershock interaction. *Science* 259 (5092), 210–213.
- Bock, K., Branquet, Y., Boulvais, P., Duretz, T., 2024. Surface-derived fluid percolation along detachment systems enhanced by syn-kinematic granites: uranium mineralization as an application. *Earth Sci. Bull.* 195, 13.
- Brocher, T.M., 2005. Empirical relations between elastic wavespeeds and density in the Earth's crust. *Bull. Seismol. Soc. Am.* 95 (6), 2081–2092.
- Chen, B., Yu, Z., Li, L., Zheng, R., Wu, C., 2023. Surface deformation and damage of 2022 (M 6.8) Luding earthquake in China and its tectonic implications. *Open Geosci.* 15 (1), 20220490.
- Clift, P.D., Hodges, K.V., Heslop, D., Hannigan, R., Van Long, H., Calves, G., 2008. Correlation of Himalayan exhumation rates and Asian monsoon intensity. *Nat. Geosci.* 1 (12), 875–880.
- Cook, K.L., Hovius, N., Wittmann, H., Heimsath, A.M., Lee, Y.H., 2018. Causes of rapid uplift and exceptional topography of Gongga Shan on the eastern margin of the Tibetan Plateau. *Earth Planet. Sci. Lett.* 481, 328–337.
- Cubas, N., Avouac, J.P., Leroy, Y.M., Pons, A., 2013. Low friction along the high slip patch of the 2011 Mw 9.0 Tohoku-Oki earthquake required from the wedge structure and extensional splay faults. *Geophys. Res. Lett.* 40, 4231–4237.
- Dai, L., Fan, X., Wang, X., Fang, C., Zou, C., Tang, X., Xu, Q., 2023. Coseismic landslides triggered by the 2022 Luding MS 6.8 earthquake, China. *Landslides* 20 (6), 1277–1292.
- Dieterich, J.H., Smith, D.E., 2009. Nonplanar faults: Mechanics of slip and off-fault damage. *Pure Appl. Geophys.* 166, 1799–1815.
- Feng, J., Kong, J., Kang, H., Zhang, W., Zhao, Y., 2018. Relocation and focal mechanism of Sichuan Luding earthquake sequence in March 2016. *Prog. Geophys.* 33 (2), 451–460.
- Gong, W., Ye, L., Qiu, Y., Lay, T., Kanamori, H., 2022. Rupture directivity of the 2021 Mw 6.0 Yangbi, Yunnan earthquake. *J. Geophys. Res. Solid Earth* 127 (9) e2022JB024321.
- Guo, R., Li, L., Zhang, W., Zhang, Y., Tang, X., Dai, K., Wang, J., 2023. Kinematic slip evolution during the 2022 Ms 6.8 Luding, China, earthquake: Compatible with the preseismic locked patch. *Geophys. Res. Lett.* 50 (5) e2023GL103164.
- Han, B., Liu, Z., Chen, B., Li, Z., Yu, C., Zhang, Y., Peng, J., 2023. Coseismic deformation and slip distribution of the 2022 Luding Mw 6.6 earthquake revealed by InSAR observations. *Geom. Inform. Sci. Wuhan Univer.* 48 (1), 36–46.
- Hardebeck, J.L., Harris, R.A., 2022. Earthquakes in the shadows: why aftershocks occur at surprising locations. *The Seismic Record* 2 (3), 207–216.
- Hardebeck, J.L., Okada, T., 2018. Temporal stress changes caused by earthquakes: a review. *J. Geophys. Res. Solid Earth* 123, 1350–1365.
- Hartzell, S.H., Heaton, T.H., 1983. Inversion of strong ground motion and teleseismic waveform data for the fault rupture history of the 1979 Imperial Valley, California, earthquake. *Bull. Seismol. Soc. Am.* 73 (6A), 1553–1583.
- Houston, H., 2015. Low friction and fault weakening revealed by rising sensitivity of tremor to tidal stress. *Nat. Geosci.* 8 (5), 409–415.
- Ingebritsen, S.E., Manning, C.E., 2010. Permeability of the continental crust: dynamic variations inferred from seismicity and metamorphism. *Geofluids* 10, 193–205.
- Jiang, G., Xu, X., Chen, G., Liu, Y., Fukahata, Y., Wang, H., Xu, C., 2015. Geodetic imaging of potential seismogenic asperities on the Xianshuihe-Anninghe-Zemuhe fault system, Southwest China, with a new 3-D viscoelastic interseismic coupling model. *J. Geophys. Res. Solid Earth* 120 (3), 1855–1873.
- Jiang, F., Chen, X., Unsworth, M.J., Cai, J., Han, B., Wang, L., Tang, J., 2022. Mechanism for the uplift of Gongga Shan in the southeastern Tibetan Plateau constrained by 3D magnetotelluric data. *Geophys. Res. Lett.* 49 (9) e2021GL097394.
- Kikuchi, M., Kanamori, H., 1991. Inversion of complex body waves—III. *Bull. Seismol. Soc. Am.* 81 (6), 2335–2350.
- King, G.C., Stein, R.S., Lin, J., 1994. Static stress changes and the triggering of earthquakes. *Bull. Seismol. Soc. Am.* 84 (3), 935–953.
- Li, H., Zhang, Y., 2013. Zircon U–Pb geochronology of the Konggar granitoid and migmatite: Constraints on the Oligo-Miocene tectono-thermal evolution of the Xianshuihe fault zone, East Tibet. *Tectonophysics* 606, 127–139.
- Li, T.S., Du, Q.F., Zhang, C., You, Z., 1997. The active Xianshuihe fault zone and its seismic risk assessment. Chengdu Cartographic Publishing House, Chengdu.
- Li, Y., Nocquet, J.M., Shan, X., Jian, H., 2021. Heterogeneous interseismic coupling along the Xianshuihe-Xiaojiang fault system, eastern Tibet. *J. Geophys. Res. Solid Earth* 126 (11) e2020JB021187.
- Li, Y., Zhao, D., Shan, X., Gao, Z., Huang, X., Gong, W., 2022. Coseismic slip model of the 2022 Mw 6.7 Luding (Tibet) earthquake: Pre- and post-earthquake interactions with surrounding major faults. *Geophys. Res. Lett.* 49 (24) e2022GL102043.
- Li, C.Y., Sun, K., Ma, J., Li, J.J., Liang, M.J., Fang, L.H., 2023. The 2022 Mw 6.8 Luding earthquake: a complicated event by faulting of the Moxi segment of the Xianshuihe fault zone. *Seismol. Geol.* 44 (6), 1648–1666.
- Liang, H., Wu, Y., Shao, Z., Li, J., Li, Y., Yi, S., Chen, C., 2023. Coseismic slip and deformation mode of the 2022 Mw 6.5 Luding earthquake determined by GPS observation. *Tectonophysics* 865, 230042.
- Liu, C., Lay, T., Brodsky, E.E., Dascher-Cousineau, K., Xiong, X., 2019. Coseismic rupture process of the large 2019 Ridgecrest earthquakes from joint inversion of geodetic and seismological observations. *Geophys. Res. Lett.* 46 (21), 11820–11829.
- Liu, Y., Yu, Z., Zhang, Z., Yao, H., Wang, W., Zhang, H., Fang, L., 2023b. The high-resolution community velocity model V2.0 of Southwest China, constructed by joint body and surface wave tomography of data recorded at temporary dense arrays. *Sci. China Earth Sci.* 66 (10), 2368–2385.
- Liu, Z., Li, J., Su, J., Yu, Z., Huang, C., Qi, Y., Wang, W., 2023a. Auto-building of aftershock sequence and seismicity analysis for the 2022 Luding, Sichuan, MS 6.8 earthquake. *Chin. J. Geophys.* 66 (5), 1976–1990.
- Miller, S.A., 2020. Aftershocks are fluid-driven and decay rates controlled by permeability dynamics. *Nat. Commun.* 11, 5787.
- Okada, Y., 1985. Surface deformation due to shear and tensile faults in a half-space. *Bull. Seismol. Soc. Am.* 75 (4), 1135–1154.
- Searle, M.P., Roberts, N.M., Chung, S.L., Lee, Y.H., Cook, K.L., Elliott, J.R., Weller, O.M., St-Onge, M.R., Xu, X.W., Tan, X.B., Li, K., 2016. Age and anatomy of the Gongga Shan batholith, eastern Tibetan Plateau, and its relationship to the active Xianshuihe fault. *Geosphere* 12 (3), 948–970.
- Shao, Z., Wu, Y., Ji, L., Diao, F., Shi, F., Li, Y., Li, X., 2023. Assessment of strong earthquake risk in the Chinese mainland from 2021 to 2030. *Earthquake Res. Adv.* 3 (1), 100177.
- Shimazaki, K., 1986. Small and large earthquakes: the effects of the thickness of seismogenic layer and the free surface. *Earthquake Source Mech.* 37, 209–216.

- Sibson, R.H., 1994. Crustal stress, faulting and fluid flow. *Geol. Soc. Lond. Spec. Publ.* 78, 69–84.
- Simpson, G., 2024. Model constraints on infiltration of surface-derived fluids deep into the brittle crust. *Geophys. J. Int.* 239 (1), 646–661.
- Sun, X., Wang, P., 2005. How old is the Asian monsoon system?—Palaeobotanical records from China. *Palaeogeogr. Palaeoclimatol. Palaeoecol.* 222 (3–4), 181–222.
- Toda, S., Stein, R.S., 2022. Central shutdown and surrounding activation of aftershocks from megathrust earthquake stress transfer. *Nat. Geosci.* 15 (6), 494–500.
- Toda, S., Stein, R.S., Sevilgen, V., Lin, J., 2011. Coulomb 3.3 Graphic-rich deformation and stress-change software for earthquake, tectonic, and volcano research and teaching—user guide. US Geological Survey open-file report 1060 (2011), 63.
- Wang, K., Hu, Y., 2006. Accretionary prisms in subduction earthquake cycles: the theory of dynamic Coulomb wedge. *J. Geophys. Res. Solid Earth* 111 (B6).
- Wang, K., Hu, Y., Von Huene, R., Kukowski, N., 2010. Interplate earthquakes as a driver of shallow subduction erosion. *Geology* 38 (5), 431–434.
- Wen, X.Z., Ma, S.L., Xu, X.W., He, Y.N., 2008. Historical pattern and behavior of earthquake ruptures along the eastern boundary of the Sichuan-Yunnan faulted-block, southwestern China. *Phys. Earth Planet. Inter.* 168 (1–2), 16–36.
- Wessel, P., Luis, J.F., Uieda, L., Scharroo, R., Wobbe, F., Smith, W.H., Tian, D., 2019. The generic mapping tools version 6. *Geochem. Geophys. Geosyst.* 20 (11), 5556–5564.
- Yang, Z., Dai, D., Zhang, Y., Zhang, X., Liu, J., 2022. Rupture process and aftershock mechanisms of the 2022 Luding M6.8 earthquake in Sichuan, China. *Earthquake Sci.* 35, 1–2.
- Ye, L., Lay, T., Kanamori, H., Rivera, L., 2016. Rupture characteristics of major and great ($M_w \geq 7.0$) megathrust earthquakes from 1990 to 2015: 1. Source parameter scaling relationships. *J. Geophys. Res. Solid Earth*, 121 (2), 826–844.
- Yuan, W., Ran, G., Zhang, H., 2015. Genetic analysis of Hailuoguo hot spring. *China Mining Magazine (in Chinese)* 24 (4), 83–87.
- Zhang, L., Zhou, Y., Zhang, X., Zhu, A., Li, B., Wang, S., Fang, L., 2023a. 2022 Mw 6.6 Luding, China, earthquake: a strong Continental Event Illuminating the Moxi Seismic Gap. *Seismol. Res. Lett.* 94, 2129–2142.
- Zhang, J., Wang, X., Chen, L., Liu, J., 2024. Seismotectonics and seismogenesis of the 2022–2023 Sichuan Luding Ms6.8, Ms5.0 and Ms5.6 earthquake sequences. *Chin. J. Geophys.* 67(4), 1471–1486. (in Chinese).
- Zhang, P., Deng, Q., Zhang, G., Ma, J., Gan, W., Min, W., Wang, Q., 2003. Active tectonic blocks and strong earthquakes in the continent of China. *Sci. China Series D: Earth Sci. (in Chinese)* 46, 13–24.
- Zhang, X., Feng, W., Li, D., Yin, F., Yi, L., 2021. Diverse rupture processes of the 2014 Kangding, China, earthquake doublet (M_w 6.0 and 5.7) and driving mechanisms of aftershocks. *Tectonophysics* 820, 229118.
- Zhang, Y., Guo, R., Sun, H., Liu, D., Zahradník, J., 2023b. Asymmetric Bilateral Rupture of the 2022 Ms 6.8 Luding Earthquake on a Continental Transform Fault, Tibetan Border, China. *Seismol. Res. Lett.* 94 (5), 2143–2153.
- Zhao, L.S., Helmberger, D.V., 1994. Source estimation from broadband regional seismograms. *Bull. Seismol. Soc. Am.* 84 (1), 91–104.
- Zhao, X., Xiao, Z., Wang, W., Li, J., Zhao, M., Chen, S., Tang, L., 2023. Fine seismogenic fault structures and complex rupture characteristics of the 2022 M6.8 Luding, Sichuan earthquake sequence revealed by deep learning and waveform modeling. *Geophys. Res. Lett.* 50 (18) e2023GL102976.
- Zheng, X., Yao, Z., Liang, J., Zheng, J., 2010. The role played and opportunities provided by IGP DMC of China National Seismic Network in Wenchuan earthquake disaster relief and researches. *Bull. Seismol. Soc. Am.* 100 (5B), 2866–2872.
- Zhu, L., Ben-Zion, Y., 2013. Parametrization of general seismic potency and moment tensors for source inversion of seismic waveform data. *Geophys. J. Int.* 194 (2), 839–843.
- Zou, R., Wang, J., Zhao, X., Fang, Z., Chen, K., Fang, R., Wang, Q., 2024. Slip model of the 2022 Mw 6.6 Luding earthquake from inversion of GNSS and InSAR with Sentinel-1. *Seismol. Res. Lett.* 95 (3), 1599–1609.